ACS NANO
Cite This: ACS Nano XXXX, XXX, XXX−XXX
www.acsnano.org

ARTICLE

Self-Powered Wind Sensor System for Detecting Wind Speed and Direction Based on a Triboelectric Nanogenerator

Jiyu Wang,[†,‡,⊥] Wenbo Ding,[†,⊥] Lun Pan,[†,⊥] Changsheng Wu,[†] Hua Yu,[†] Lijun Yang,[‡] Ruijin Liao,*[,‡] and Zhong Lin Wang*[,†,§]

[†]School of Material Science and Engineering, Georgia Institute of Technology, Atlanta, Georgia 30332, United States

[‡]State Key Laboratory of Power Transmission Equipment and System Security and New Technology, Chongqing University, Shapingba, Chongqing 400044, People's Republic of China

[§]Beijing Institute of Nanoenergy and Nanosystems, Chinese Academy of Sciences, National Center for Nanoscience and Technology (NCNST), Beijing 100083, People's Republic of China

Supporting Information

ABSTRACT: **The development of the Internet of Things has brought new challenges to the corresponding distributed sensor systems. Self-powered sensors that can perceive and respond to environmental stimuli without an external power supply are highly desirable. In this paper, a self-powered wind sensor system based on an anemometer triboelectric nanogenerator (a-TENG, free-standing mode) and a wind vane triboelectric nanogenerator (v-TENG, single-electrode mode) is proposed for simultaneously detecting wind speed and direction. A soft friction mode is adopted instead of a typical rigid friction for largely enhancing the output performance of the TENG. The design parameters including size, unit central angle, and applied materials are optimized to enhance sensitivity, resolution, and wide measurement scale. The optimized a-TENG could deliver an open-circuit voltage of 88 V and short-circuit current of 6.3 μA, corresponding to a maximum power output of 0.47 mW (wind speed of 6.0 m/s), which is capable of driving electronics for data transmission and storage. The current peak value of the a-TENG signal is used for analyzing wind speed for less energy consumption. Moreover, the output characteristics of a v-TENG are further explored, with six actual operation situations, and the v-TENG delivers fast response to the incoming wind and accurately outputs the wind direction data. As a wind sensor system, wind speed ranging from 2.7 to 8.0 m/s can be well detected (consistent with a commercial sensor) and eight regular directions can be monitored. Therefore, the fabricated wind sensor system has great potential in wireless environmental monitoring applications.**

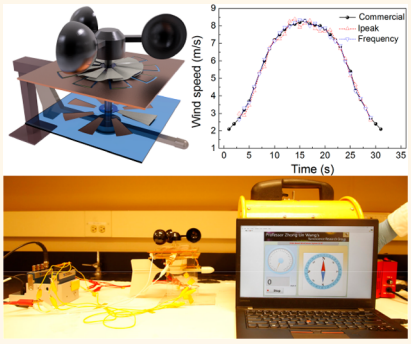

KEYWORDS: *Internet of Things, triboelectric nanogenerator, wind speed and direction sensor, freestanding mode, single-electrode mode*

The Internet of Things (IoT) is a promising concept for the realization of integrating the physical and digital world by using widely distributed sensors for seamlessly exchanging and processing information that can be used anywhere and anytime.[1,2] The establishment of IoT requires billions or trillions of decentralized sensors that can monitor every aspect of human lives reliably and autonomously. As the development of distributed nodes in networks is increasing rapidly, the deficiencies of conventional battery-based sensors such as limited lifetime, large package size, low device maintainability, and risk of environment pollution are challenging.[3−5] Thus, self-powered devices that harvest energy from the surroundings have been highlighted as a promising and sustainable solution to break through the restraints of conventional power supply. Among various energy-harvesting devices, triboelectric nanogenerators (TENGs) based on Maxwell's displacement current are considered as the most effective way to convert various types of mechanical energy in the natural environment.[6−11] Compared with piezoelectric nanogenerators, TENGs exhibit notable characteristics of light weight, easy fabrication, low cost, and high efficiency.[12] Taking advantage of this technology, TENGs recently have been widely utilized to effectively scavenge most types of energy, such as mechanical energy,[13−16] wind energy,[17−19] and water energy,[20−24] especially at lower frequencies.[25−27] In this regard, the concept of utilizing TENGs as a self-powered active sensor

Received: February 27, 2018
Accepted: March 29, 2018
Published: March 29, 2018

DOI: 10.1021/acsnano.8b01532
ACS Nano XXXX, XXX, XXX−XXX

can be a practical and effective strategy to lay the foundation for the development and expansion of the IoT.

A wind sensor system can be regarded as the epitome of the IoT. A sensor system detecting wind speed and direction can play a critical role in various fields, such as weather forecasting and environment monitoring, due to its simple structure, compact size, and fast response. The data monitored and diagnosed by the sensor systems are a key part for its precise prediction. Therefore, numerous sensor systems should be reliably operated and widely installed in order to collect accurate and comprehensive information. However, battery-based sensors with the drawbacks of limited lifetime and low maintainability cannot ensure a safe and reliable operation, and numerous installed sensors with batteries have a large impact on the environment and is a waste of resources.[28,29] Herein, a self-powered wind sensor system based on TENGs that operates reliably, sustainably, and independently is proposed to resolve such limitations.

The wind-driven TENGs generate electricity from wind energy through the coupling of triboelectrification and electrostatic induction. The periodic friction motion between two different surfaces with oppositely polarized triboelectric charges can cyclically change the induced potential difference across two electrodes, thus driving the alternating flow of electrons through an external load.[30,31] The amount of triboelectric charge is closely related to the force of friction provided by wind energy. However, the friction mechanism as the core principle of TENGs is contraindicated as a means of collecting low wind speed. The force driven by low wind speed cannot provide continuous kinetic energy for a complete friction cycle of a TENG. In this case, it is challenging for a TENG sensor to monitor the wind data under the circumstance of low wind speed. Previous research concentrated on enlarging the size of sensors or assembling a turbo charger to enhance the torque under low wind speed at the cost of compact size.[32−34] Others that focused on modifying the structure of the sensor such as using a flutter-driven mode[35−38] may have limitations on stable signal output. In this regard, a comprehensive design strategy to obtain both a miniaturized device area and high performance should be formulated.

In this work, a TENG-based wind sensor system that can detect wind speed and wind direction simultaneously is proposed. The sensor system consists of two main parts, with the upper anemometer TENG (a-TENG) used for wind speed detection and the lower wind vane TENG (v-TENG) for monitoring wind direction. The a-TENG is designed on the principle of a freestanding mode,[39,40] while the v-TENG is based on the single-electrode mode.[41,42] Specifically, a soft friction mode (based on soft polymer films) instead of a rigid friction mode is used to contact and rub the Cu electrodes because of the lower frictional resistance and better durability. On the basis of this design, an open-circuit voltage (V_{oc}) of 88 V and short-circuit current (I_{sc}) of 6.3 μA have been achieved, corresponding to a maximum power output of 0.47 mW, which is capable of data transmission and data storage. Furthermore, the v-TENG could deliver fast response to the incoming wind and accurately output the wind direction data. Also, data transmission and storage units are integrated with the wind sensor system, which is important progress toward the practical applications in the development of the IoT.

RESULTS AND DISCUSSION

Structure and Working Mechanism of the Fabricated TENG. The sensor system has a multilayered structure, which consists of mainly two parts, as illustrated in Figure 1a−c. The anemometer TENG (a-TENG) part is employed for wind speed detection, while the wind vane TENG (v-TENG) part is for wind direction monitoring.

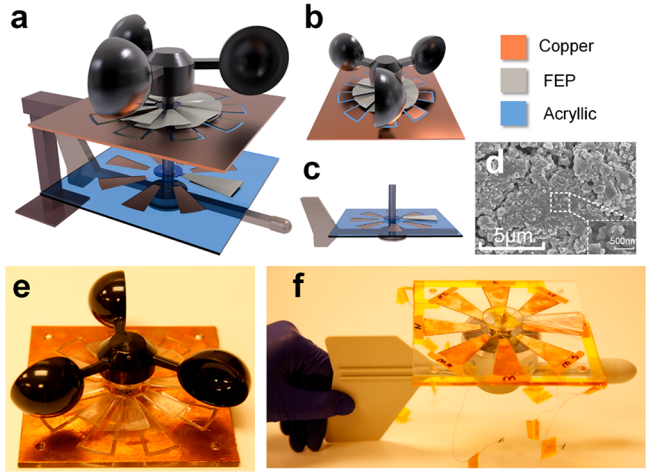

Figure 1. Structural design of TENG-based wind sensor system. (a) Schematic illustrations of the wind sensor system, which has two parts, which are (b) an a-TENG consisting of wind cups, a stator, and a rotator adhered with FEP films and (c) a v-TENG consisting of a vane connected with a pie-shaped rotator and a stator. (d) SEM image of the FEP film. Photographs of (e) as-fabricated a-TENG and (f) v-TENG.

As shown in Figure 1b, the a-TENG is constituted by three parts, *i.e.*, wind cups, rotator, and stator. The wind cups used for harvesting wind will drive the rotator. The rotator with fluorinated ethylene propylene (FEP) film acts as a triboelectric surface, and the rotator is a collection of radially arrayed sectors separated by equal-degree intervals in between. With each sector unit having a central angle of 10°, the rotator has a total of nine units. One side of the FEP film is fixed at the spoke of each sector, leaving the other side free-standing. The free-standing side will be bent and appropriately contact the stator, which is composed of two complementary-patterned electrode networks that are disconnected by fine trenches in between. Having the same pattern as that of the rotator, each network on the stator is formed by a radial array of sectors that are mutually connected at one end; thus the inner networks and the outer networks can be regarded as two terminal electrodes. As each adjacent network belongs to the opposite electrode, the distance between the rotator and stator and the shape of FEP film should be adjusted properly, making the free-standing side of the FEP film completely contact only one network without covering the adjacent network.

The v-TENG with two parts is shown in Figure 1c. One is a vane connected with a pie-shaped rotator used for indicating the wind direction, and the other one is a compass on which the Cu electrodes are independent. Each electrode with a central angle of 30° is radially distributed on the compass, indicating eight directions. The pie-shaped rotator is totally covered by the FEP film and has the same size as one single Cu electrode. The vane will drive the rotator blade; thus the FEP film will sweep the electrodes, which can produce an output

DOI: 10.1021/acsnano.8b01532
ACS Nano XXXX, XXX, XXX−XXX

signal. Each electrode is regarded as one terminal electrode and is connected with an individual external channel. Based on the signals occurring at various external channels, the current status and moving trail of the rotator can be analyzed for wind direction monitoring. A scanning electron microscope (SEM) image of the FEP film can be seen in Figure 1d. As exhibited in Figure 1e,f, the device has the dimensions 12 cm × 12 cm × 15 cm (L × W × H). This rational design not only leads to structural simplicity but also accounts for excellent portability.

Figure 2a illustrates the electricity generation process under the relative rotation motions between the FEP films on the

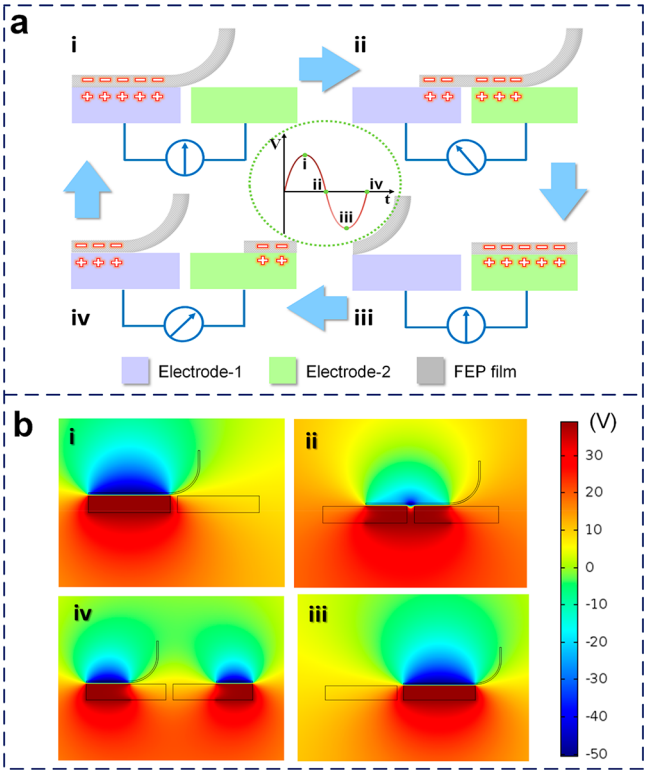

Figure 2. (a) Schematic working principle of an a-TENG in the soft friction mode (i–iv) and (b) the simulated potential distributions for the a-TENG at four different displacements by COMSOL employing the finite element method (i–iv).

rotator and the Cu electrodes on the stator, through which alternating current is provided to the external load. We define the first contacted electrode by the FEP film as electrode-1, and the electrode that is next to electrode-1 as electrode-2. At the initial state, the FEP film is at the position fully overlapped with electrode-1, resulting in negative charges generated by the triboelectrification. The negative charges on the FEP surface should be equal to the positive charges in the Cu electrode. Thus, the positive charges in the loop will accordingly be attracted to the upper surface of electrode-1 due to electrostatic induction. When the FEP film slides toward electrode-2, the positive charges in the loop will flow from electrode-1 to electrode-2 *via* the load to screen the local field of the nonmobile negative charges on the FEP film. When the FEP film reaches the overlapping position of electrode-2, all of the positive charges will be driven to electrode-2, which is regarded as the first half-cycle of electricity generation. After that, as the rotator keeps spinning, the FEP film continues to fully contact the surface of the next adjacent electrode. Since each adjacent electrode is a part of the opposite networks, respectively, a reverse current is subsequently formed. This is the second half of the electricity generation process.

Based on the disk structure, the amount of charges in this transport process can be expressed by eq 1.[43]

$$Q = \frac{\alpha_0}{180}\sigma\pi(r_2^{\,2} - r_1^{\,2}) \tag{1}$$

where α_0 is the central angle of one single electrode unit (α_0 = 10°). σ is the triboelectric charge density on the FEP layer, normally equal to ~200 μC·m^{-2}.[44] r_2 and r_1 are the outer radius and inner radius of the stator, which are 0.5 and 0.005 m, respectively. By substituting the known parameters into eq 1, the transferred charge is theoretically estimated to be ~40 nC. Therefore, an alternating electricity is generated as a result of the periodically changing electric field, which has a frequency calculated by eq 2.

$$f = \frac{180\nu}{\alpha_0} \tag{2}$$

where ν is the rotation rate (r s^{-1}).

In the open-circuit condition, electrons cannot transfer between electrodes without the load. The open-circuit voltage (V_{oc}) is then defined as the electric potential difference between the two electrodes. The electrostatic induction process can produce V_{oc} signals as the positive charges on the electrode are orderly screened by the negative triboelectric charges on the FEP film. Therefore, as shown in the inset of Figure 2a, the maximum V_{oc} value appears at the states of i and iii when the positive charges on one of the electrodes are fully screened by the negative charges. Such a voltage then diminishes as the rotator spins. Once the rotator passes the middle position of the two electrodes, the V_{oc} value reaches the zero-crossing point, and V_{oc} with the opposite polarity starts to build up until the rotator reaches the next middle position. Further rotation induces the V_{oc} to change in a reversed way because of the periodic structure. For a further understanding, the continuous variation of the V_{oc} is visualized through finite-element simulation using COMSOL, as shown in Figure 2b. In addition, the electricity signal produced in the v-TENG shares a similar principle with that in the a-TENG.

Characteristics of the a-TENG. To characterize the electrical output performance of the a-TENG, a wind turbine system with adjustable wind speed controlled by applied voltage is established to simulate the wind energy. The measurement was performed under different wind speeds, and the minimum start-up wind speed for the a-TENG is 2.7 m/s. From Figure 3a–c, V_{oc} as well as the transferred charge quantity (Q_{sc}) remains almost constant (80 V and 35 nC) with wind speeds increasing from 2.7 to 8.0 m/s, while the short-circuit current (I_{sc}) increases from 0.2 to 6.3 μA, exhibiting a positively proportional relationship with wind speed. According to the theory of a freestanding triboelectric-layer-based nanogenerator, the a-TENG could be considered as a capacitor with a constant transferred charge through both electrodes. The V_{oc} of the a-TENG is directly related to the transferred charges between two electrodes, which depends on the maximum overlapping area of the FEP film and the electrode. Therefore, the quantity of V_{oc} and Q_{sc} remain almost constant with the variation of wind speed. However, the I_{sc} will be varied as the wind speed changes, which is regarded as the core working mechanism for the a-TENG. The output current is defined as the rate of flow of charges (Q), given by eq 3.

DOI: 10.1021/acsnano.8b01532
ACS Nano XXXX, XXX, XXX–XXX

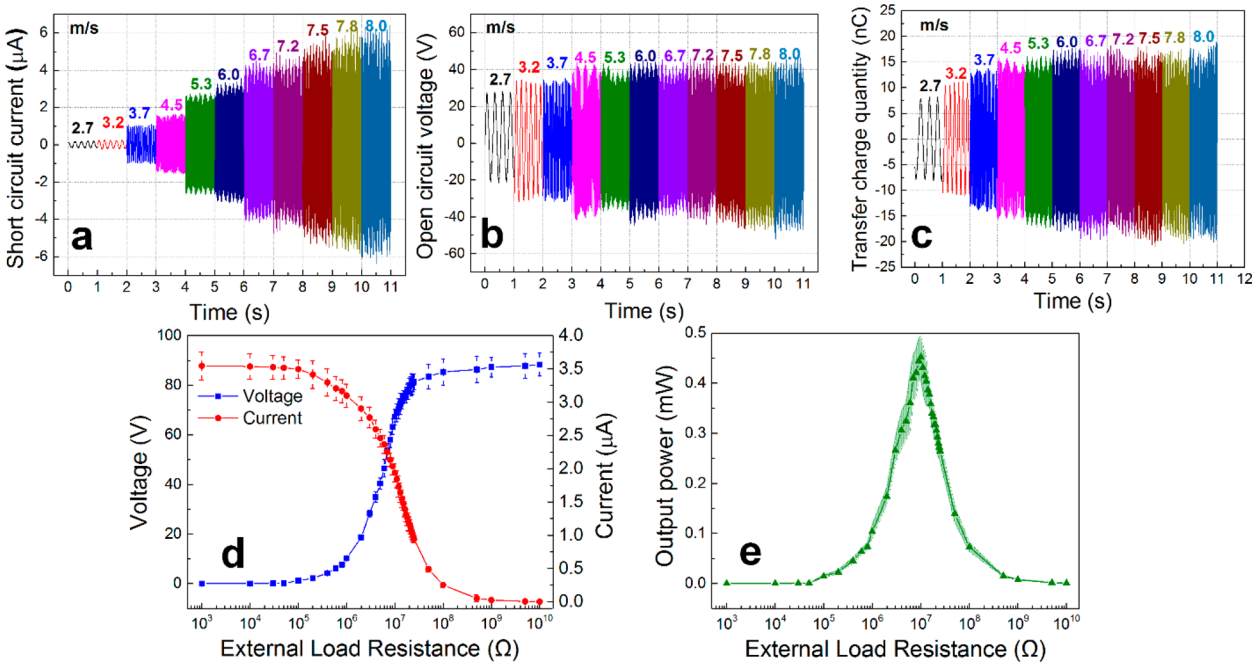

Figure 3. Electric measurements of the a-TENG. (a) I_{sc}, (b) V_{oc}, and (c) Q_{sc} under different wind speeds. (d) Variation of the output current, voltage, and (e) peak power with the external loading resistance (under a wind speed of 6.0 m/s).

$$I = \frac{dQ}{dt} \tag{3}$$

As the transferred charges are constant, whereas the rotation time is varied relating to the different wind speeds, the output current would correspondingly change. The I_{sc} experiences a rapid growth, then increases slightly in the same upward trend as the wind speed curve, which is controlled by the applied voltage, as shown in Supplementary Figure 1. Once an external load is applied, the amplitude of the output current drops as the load resistance increases, while the amplitude of the output voltage follows a reverse trend (Figure 3d). At a wind speed of 6.0 m/s, the instantaneous output power is maximized at a load resistance of ~10 MΩ, corresponding to a peak power of 0.47 mW (Figure 3e).

It is noteworthy that there is a slight increase in both V_{oc} and Q_{sc} quantity as the wind speed increases, resulting from the deformation degree of the FEP film. For the bending effect of the FEP film, since the electrodes are radially arrayed on the stator, the electrode area on the outer edge is larger than that toward the center. The parts of the electrodes near the center have very small areas as their gaps, leading to the possibility of mistaken connection for the FEP film. Under lower wind speed, the free-standing side of the FEP film will be deformed naturally due to the gravity and mistakenly contact the adjacent electrode at the overlapping position. Since the negative charges on the film cannot be fully screened by the positive charges on only one electrode, the electric potential difference will accordingly decrease. As the wind speed accelerates, the buoyancy caused by the air flow will partly balance the gravity, making the FEP film slightly deformed and fully contact the electrode without mistaken connection, and the electric potential difference thus slightly increases. In addition, a typical rigid friction mode is designed to output an electric signal for a better comparison, as shown in Supplementary Figure 2. There are no obvious changes in the voltage values as well as the transferred charge quantity with the increase in wind speed for the rigid friction mode, confirming our assumption on the effect of deformation degree of the FEP film. Also, it is clear to see the output voltage values obtained by the rigid friction mode are close to that obtained by the soft friction mode, which means the typical rigid friction mode can be well substituted by the soft friction without any discernible electrical output reductions.

The a-TENG designed as an electric sensor needs favorable sensitivity and resolution and a wide measurement scale. Design parameters, especially the size, the unit central angle, and the applied materials, can also largely influence the characteristics of the TENG-based sensor. Specifically, the size is altered by doubling the radial length of the rotator, and the area of the FEP film is expanded accordingly (Figure 4a). The pairs of electrodes are also modified as a representative of the unit central angle increase or decrease, as schematically shown in Figure 4b. The physical images of a-TENGs with various design parameters can be found in Supplementary Figure 3. Since the peak value and frequency of the output current are determined by the wind speed, the relationship between those two dependent variables and the wind speed is respectively revealed in Figure 4c,d.

As demonstrated in Figure 4c, the curves for 9r-small (nine pairs of electrodes with short radial length of the rotator) and 9r-long (nine pairs of electrodes with doubled radial length of the rotator) present a similar upward trend. The current peak value of 9r-long rises faster than that of 9r-small owing to the increased triboelectric charges generated by the extended friction area. Thus, the sensor with doubled radial length of the rotator has a better measurement resolution. However, the weight of the sensor increases as the radial length is extended, which limits the start-up of the rotator. As a result, the minimum start-up wind speed of 9r-small is 2.7 m/s, while that of 9r-long is 3.2 m/s, which is discarded due to the weaker sensitivity. For a comparison of the electrode pairs, the sensors with 5, 9, 18, and 36 pairs of electrodes can operate at the same minimum start-up wind speed, which ensures a favorable

DOI: 10.1021/acsnano.8b01532
ACS Nano XXXX, XXX, XXX−XXX

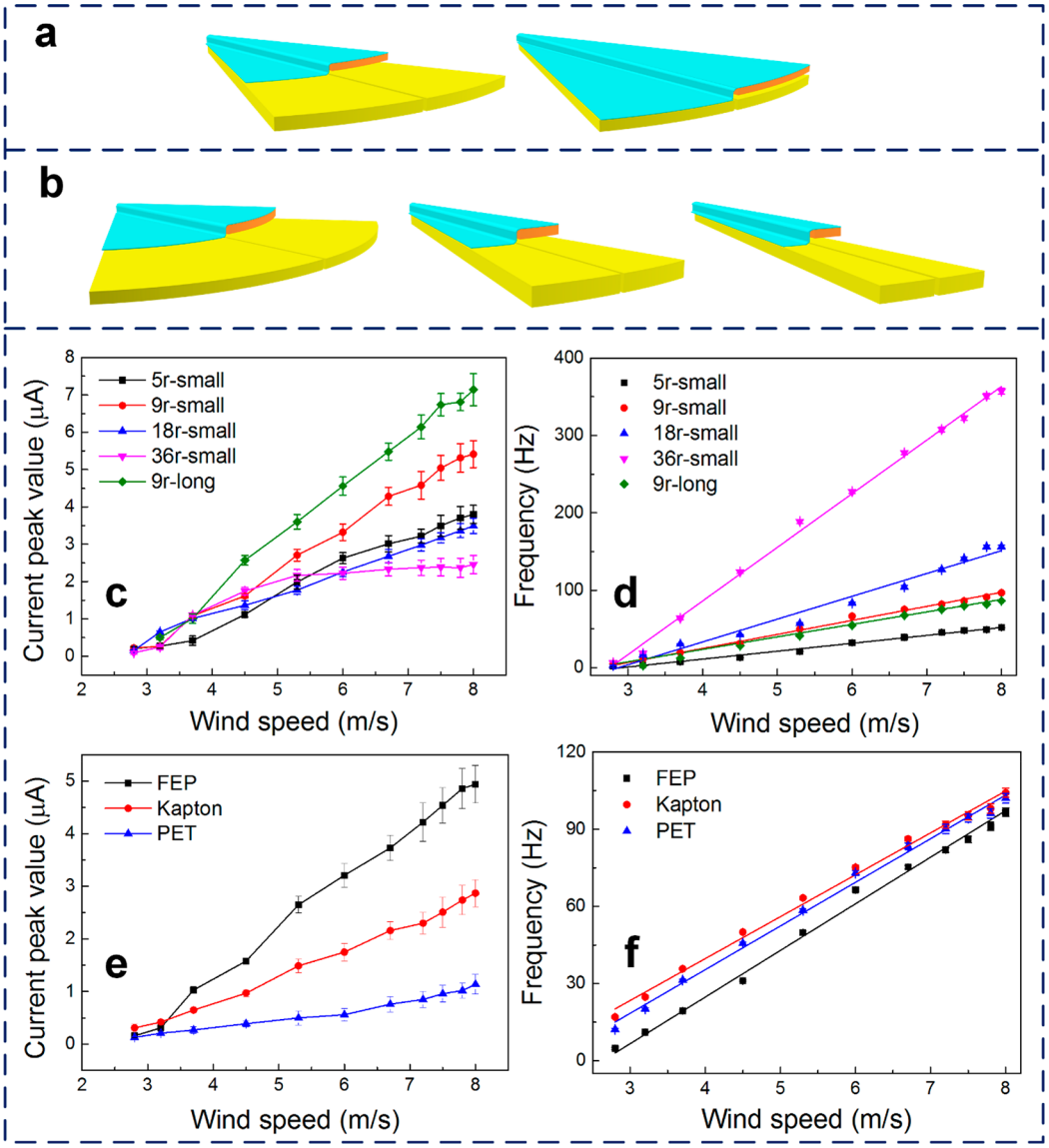

Figure 4. Design parameters that influence the characteristics of an a-TENG. Schematic illustrations of an a-TENG based on (a) nine pairs of electrodes with short radial length and long radial length of the rotator; (b) five, 18, and 36 pairs of electrodes with same short radial length of the rotator. (c) Current peak values and (d) frequencies of various designed a-TENGs *vs* wind speed. (e) Current peak values and (f) frequencies of a-TENGs (9r-small) fabricated by different dielectric materials *vs* wind speed.

sensitivity. In contrast with other curves, the curve of 36r-small exhibits a saturated trend as the wind speed rises; that is, the current peak value climbs as the wind speed rises to 5.3 m/s, then holds steady regardless of the increased wind speed. This phenomenon is inconsistent with the principle of electricity generation of a TENG, in which the output current would correspondingly change with the varied flow rate of transferred charges. The reason for this is because the sectors of the rotator matched with 36 pairs of electrodes are closely radial arrayed, with a very short distance between each FEP film fixed on each section. As the rotation speed rises, more triboelectric charges on the FEP surface easily interact with each other by distorting the electric field of the neighbors. Therefore, the flow rate of transferred charges is largely restricted. This particular phenomenon happens only in the soft friction mode, where the films naturally hang down from the rotator. In this case, the sensor with 36 pairs of electrodes is discarded because of the lack of a wide measurement scale.

Furthermore, the curves of 5r-small and 18r-small show the same upward trend as 9r-small. However, compared with 9r-small, the current peak value of 5r-small increases more slowly under low wind speed because of the lower flow rate of transferred charges, while that of 18r-small increases faster when the wind speed varies from 2.7 to 3.7 m/s, then increases slowly because of the restricted flow rate of transferred charges affected by the surface charges. The sensors with 5r-small and 18r-small both are short of high resolution, although they possess the same sensitivity and measurement scale as that for 9r-small.

As shown in Figure 4d, the frequency variation trend is linearly related to the electrode pairs. In this case, the sensor with 36 pairs of electrodes has a favorable sensitivity, resolution, and measurement scale. Also, the sensor with nine pairs of electrodes with double the radial length of the rotator lacks this advantage since there is no significant difference except the minimum start-up wind speed between the curves of 9r-small

DOI: 10.1021/acsnano.8b01532
ACS Nano XXXX, XXX, XXX−XXX

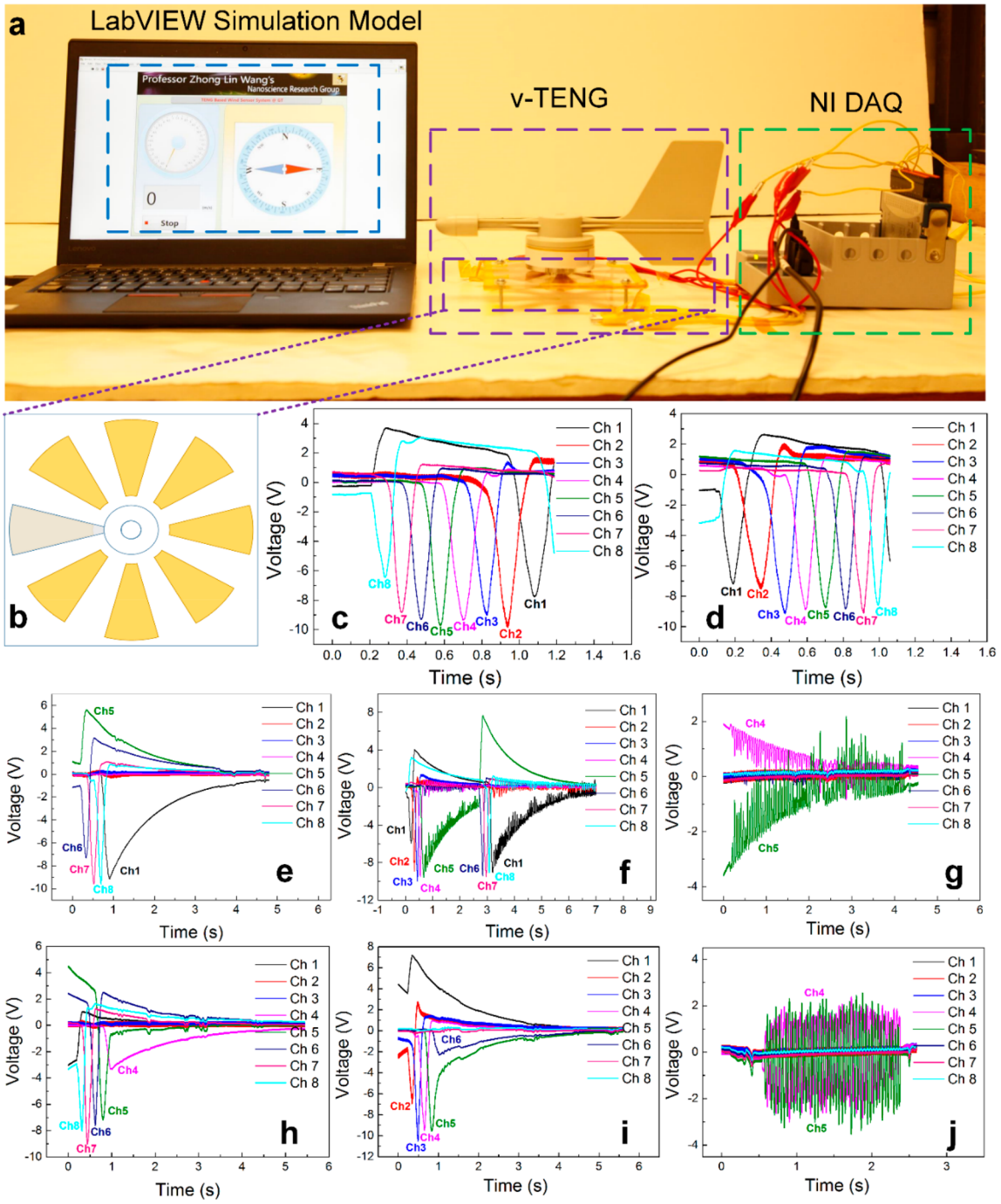

Figure 5. Output characteristics of the v-TENG. (a) Measurement platform with NI DAQ for data reading and transmission, v-TENG for reflecting the moving trail of the rotator, and programmed LabVIEW simulation for data processing. (b) Schematic illustration of the v-TENG on which the electrodes are radially arrayed on the stator. The overlaying output voltage signals obtained from eight channels when the rotator sweeps over the electrodes in both (c) clockwise and (d) counterclockwise directions. The output voltage signal as the wind vane (e) rotates counterclockwise from Ch6 and steadily stops at Ch1, (f) rotates counterclockwise from Ch1 and vibrates at Ch5, then rotates from Ch5, and eventually vibrates at Ch1, (g) proceeds with a reciprocating vibration at Ch5, (h) rotates clockwise and stops between Ch4 and Ch5, (i) crotates ounterclockwise and stops between Ch5 and Ch6, (j) proceeds with a reciprocating vibration between Ch4 and Ch5.

and 9r-long. However, we still adopt the sensor with nine pairs of electrodes as our final design, because the frequency analysis is not an intuitive analysis, which needs more data acquisition units, arithmetic logic units, and storage space. It will consume more power than the current peak value analysis does. Therefore, the current peak value analysis as a less energy consuming strategy is regarded as the main analytical method, while the frequency value analysis is an auxiliary analysis.

The output performance of the a-TENG also can be modified by triboelectric charge generation, which depends on the friction materials. Figure 4e,f show the electrical output of an a-TENG with different film materials, *i.e.*, FEP, Kapton, and PET, corresponding to same radial length of the rotator and pairs of electrodes. Overall, the increased rate of the current peak value presents a positive correlation to the electron affinity of the material. Thus, the FEP with a much

DOI: 10.1021/acsnano.8b01532
ACS Nano XXXX, XXX, XXX−XXX

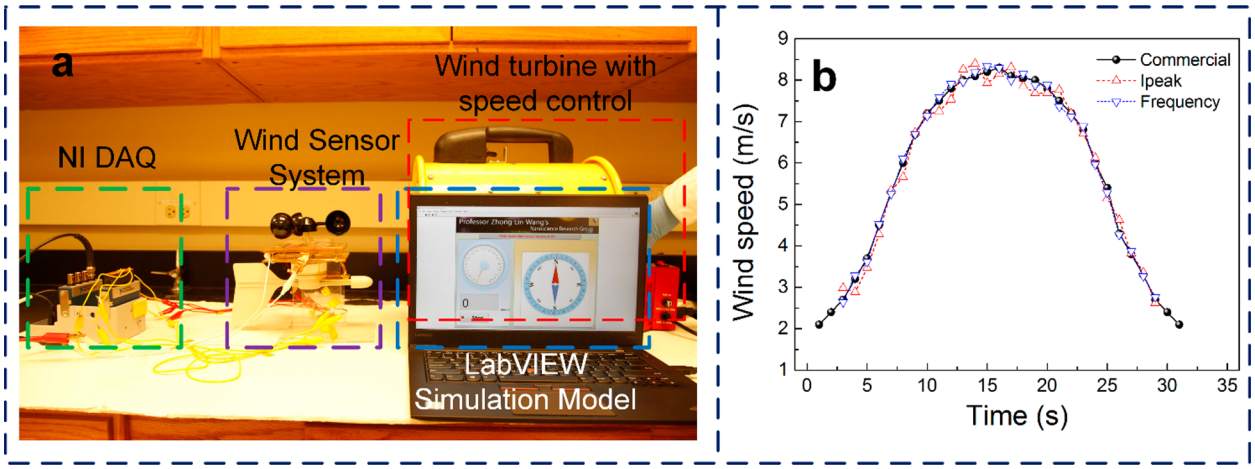

Figure 6. Demonstration of the wind sensor system for obtaining real-time wind speed. (a) Photograph of the measurement platform, in which the NI DAQ is used for data reading and transmission, the wind sensor system is composed of a-TENG and v-TENG and fixed on an acrylic support, the wind turbine controlled by miniature transformer is employed for wind power output, and the LabVIEW simulation model is programmed for data processing. (b) Real-time wind speed curves detected by a commercial wind speed sensor and a fabricated wind sensor system with both the current peak value method and the frequency method.

stronger ability to obtain electrons can generate more triboelectric charges, resulting in a higher current peak value of 5 μA. In addition, all the materials share a comparable increase rate, which means the ability to obtain or lose electrons is not related to the frequency of the electricity in the loop, as shown in Figure 4f. However, the frequency value of each material varies under different wind speeds, caused by the varied friction resistances and ductility factors of different materials. In addition, the FEP film has the characteristics of extremely excellent chemical compatibility, electrical reliability, and mechanical toughness. As a result, the proposed sensor system based on FEP films maintains good stability and durability, as shown in Supplementary Figure 4.

Characteristics of the v-TENG. The v-TENG as another part of the wind sensor system is designed to monitor wind direction. The pie-shaped rotator covered by the FEP film is fixed on the same axis of the vane and is driven by wind flow. The stator is used as a compass on which eight Cu electrodes are radially distributed with eight directions. In this way, eight independent signal channels are connected with the electrodes, respectively, and a particular output signal can be achieved when the FEP film sweeps over the corresponding electrode. The measurement platform is shown in Figure 5a,b, and the current status and moving trail of the rotator can be obtained for wind direction monitoring by analyzing the output signals. Figure 5c,d show the overlaying output voltage signals obtained from eight channels when the rotator sweeps over all the electrodes in both clockwise and counterclockwise directions. On the basis of the curves, we define a full wave trough as a complete process that the rotator passes through one single electrode regardless of the voltage value. Since the working mechanism of the v-TENG is based on the single-electrode mode of a TENG, the voltage value is related to the surface charges of the film, which are easily influenced by the current degree of deformation, rotation speed, and other environmental variables. It is understandable that the voltage signal of the channel occurs when the film starts to contact the corresponding electrode. Then the voltage value grows as the contact area increases and reaches a peak value when the film is at the overlapping position of the electrode. After that, the voltage value gradually decreases to zero and the output voltage signal of the next channel starts to occur. As the vane rotates counterclockwise, the signal of the first channel appears first, and the signals of the second to eighth channel sequentially appear. While the vane is in clockwise rotation, the signals of the eight channels appear in a reverse order. Movie S1 exhibits a demonstration of the v-TENG for reflecting the moving trail of the rotator.

Because of the instability and uncertainty of the wind energy, the actual operation situation of the v-TENG is much more complicated. We therefore simulate six operation situations that may happen in the real environment to investigate the practicability and accuracy of this sensor device, as shown in Figure 5e–j.

Figure 5e shows that the wind vane rotates counterclockwise from Ch6 and steadily stops at Ch1. It is clearly observed that the first wave trough signal occurs at Ch6, and the last wave trough signal occurs at Ch1 after two wave trough signals of Ch7 and Ch8. When the rotator steadily stops at the overlapping position of Ch1, no more wave trough signals appear, and the surface charges on the electrode are exponentially dissipated without friction motion. Figure 5f reflects two rotation processes where the wind vane rotates counterclockwise from Ch1 and vibrates at Ch5, then rotates from Ch5 and eventually vibrates at Ch1. The order in which different wave trough signals occur can indicate the motion of the vane. The fluctuation is clearly observed in the decay process of the surface charges when the rotator reaches the overlapping positions of Ch5 and Ch1. The fluctuation of the output voltage is the result of the triboelectric charges generated by reciprocating friction. This is a common situation in actual operation when the wind energy is multiorientational or intermittent. Figure 5g reflects that the rotator moves with a reciprocating vibration at Ch5, which may happen under a strong wind flow after a long windless interval. This situation is partly similar to the previous case. Without any wave trough signals before, the fluctuation in the decay process of the charges represents the reciprocating vibration; thus this situation can be directly recognized. The aforementioned cases simulate the actual situations in which the rotator stops at the exact position above a single electrode.

DOI: 10.1021/acsnano.8b01532
ACS Nano XXXX, XXX, XXX–XXX

The situations in which the rotator stops at the in-between position of two electrodes are also considered. Figure 5h,i reflect that the wind vane rotates clockwise, stops between Ch4 and Ch5, rotates counterclockwise, and stops between Ch5 and Ch6, respectively. This situation can be well recognized by observing the signals from two decay processes of charges simultaneously appearing on adjacent channels, and one wave trough of the signal is formed since the rotator has already passed the overlapping position of the electrode. Figure 5j shows the last situation, in which the rotator proceeds with a reciprocating vibration between Ch4 and Ch5. The fluctuations of output voltage are clearly observed on the signals of both channels, and there is no decay process of charges, which is different from Figure 5f. This case can be considered as the sliding freestanding mode of the TENG, in which the dielectric layer slides against the two electrodes, leading to the triboelectric charges being transferred between electrodes due to the electric potential difference.

It is noteworthy that when the rotator starts to slide across an electrode, a wave peak is observed on the signal of the channel connected to the electrode ahead of the contacted electrode, such as the wave peak of Ch5 in Figure 5e and the wave peak of Ch1 in Figure 5i, resulting from electrostatic induction. The triboelectric charges suddenly generated on the electrode will form an electrostatic field, and opposite charges will be induced on the adjacent electrode because of the electric potential. The electrostatic field center varies from one edge to another edge of the electrode according to the rotation direction. When the electrostatic field center shifts to another edge, the induced opposite charges on the next electrode are mostly screened by the triboelectric charges on the surface of the upcoming film, leading to little impact on the voltage signal of the next channel.

Demonstration. To demonstrate the performance of the wind sensor system in a simulated environment, the measurement platform is established and displayed in Figure 6a. The wind flow from any direction can be achieved by adjusting the orientation of the sensor system. The real-time current peak value I_{peak} and the frequency f are obtained from the real-time electrical output of the a-TENG part. The wind speed S is therefore analyzed using the statistical relationship between the I_{peak} and the incoming wind speed, and the wind direction is also monitored without mutual interference (Movie S2). In addition, the obtained frequency also can determine the wind speed S based on the relationship between the frequency of the electrical output, *i.e.*, current, voltage, and transferred charge quantity. The wind speed obtained by the frequency is regarded as an auxiliary analysis in practice because of the greater power consumption. In addition, a commercial hotwire anemometer (Testo 405i) is employed for comparison (Movie S3). The wind speed analyzed by both current peak value and frequency ways agrees well with that obtained by the hotwire anemometer, as shown in Figure 6b. Specifically, the correlation coefficients of the results obtained by a commercial sensor and a fabricated sensor are further calculated by calculating the Euclidean distance. The Euclidean distance can be expressed by eq 4 and eq 5.

$$D(C, I) = \sqrt{\sum_{i=1}^{n} (y_i - I(x_i))^2} \quad (4)$$

$$D(C, f) = \sqrt{\sum_{i=1}^{n} (y_1 - f(x_i))^2} \quad (5)$$

By substituting the related results, $D(C, I)$ is calculated as 1.1180, while $D(C, f)$ is calculated as 0.4328. Each method shows a favorable correlation with the results from the commercial sensor. The v-TENG part can deliver a fast response to the incoming wind and accurately output the wind direction data. It demonstrates that the wind sensor system can simultaneously and stably deliver information on wind speed and wind direction without mutual interference. Integrated with data transmission and storage units, all the wind information on one region can be monitored and recorded for a long time, without any power supply systems.

CONCLUSION

In summary, a self-powered wind sensor system based on a TENG has been proposed and fabricated for simultaneously monitoring of the wind speed and direction. The sensor system consists of two parts. The anemometer part (a-TENG) that harvests wind energy serves as a wind speed sensor as well as an energy supply device, while the wind vane part (v-TENG) serves as a wind direction sensor. The soft friction mode is first adopted instead of the typical rigid friction in the designed TENG, which can largely enhance the sensitivity and reduce the minimum start-up wind speed. The effects of the radial length of the rotator, pairs of electrodes, and friction materials are further explored for obtaining the optimized parameters for the fabricated wind sensor, and the optimized a-TENG delivers an open-circuit voltage of 88 V and a maximum short-circuit current of 6.3 μA, corresponding to a maximum power output of 0.47 mW at a wind speed of 6.0 m/s. The current peak value method is used as the main analytical method, while the frequency method is used as the auxiliary analytical method. A wind speed ranging from 2.7 to 8.0 m/s can be well detected by the fabricated a-TENG with a favorable sensitivity and resolution. In addition, six particular operation situations are further explored to investigate the practicability and accuracy of the v-TENG. With various output signals of all the channels, the v-TENG can deliver a fast response to the incoming wind and accurately reflect the wind direction. The fabricated wind sensor system based on a TENG has shown potential applications in wireless environmental monitoring networks, which is expected to be great progress toward practical applications in the development of the IoT and large-area climate monitoring.

EXPERIMENTAL SECTION

Fabrication of the Wind Sensor System. The fabricated wind sensor system has two main components, as illustrated in Figure 1a. The upper part is the a-TENG used for wind speed detection and energy supply. The lower part is the v-TENG for monitoring wind direction.

For the a-TENG fabrication, a 50 μm thick FEP film was cut into a fan shape to serve as the dielectric layer, also called the friction layer, and subsequently slid against the copper collecting electrode used. A laser cutter (Universal Laser Systems) was used to cut a 3 mm thick acrylic sheet into a radial shaped disc as the rotator with a central angle of 10° for each sector. One side of the FEP film was adhered to the edge of each sector, leaving the other side of film free-standing. The laser cutter was used to etch trenches on a 3 mm thick acrylic square sheet to create two complementary-patterned electrode networks. Each network was formed by a radial array of sectors with the same sector area as the rotator. Copper foil was employed to adhere on the surface of the prepared acrylic, followed by incising this foil along with the etched trenches to generate the electrode pattern on the substrate as the stator. The distance between the rotator and stator was adjusted

DOI: 10.1021/acsnano.8b01532
ACS Nano XXXX, XXX, XXX−XXX

properly to make the free-standing side of the FEP film completely contact only one network without covering the adjacent network of the substrate. Copper wires were connected to the two sectors of the disconnected network as output terminals. The wind cup was mounted on the rotator and connected with the stator using a bearing.

For the v-TENG fabrication, the laser cutter was used to cut a 3 mm thick acrylic sheet into a pie shape with a 30° central angle as the rotator. A 50 μm thick fan-shaped FEP film was circled and adhered to one side of the rotator. An acrylic rod with a 5 mm diameter was used as an axis to connect the vane and the rotator. The stator was fabricated with a 3 mm thick acrylic sheet. The laser cutter was used to etch trenches on the substrate to create eight independent regions. These regions were radially distributed with a central angle of 30°, indicating eight directions as a compass. Copper foil was cut into the same shape of the region and adhered on its surface. The vane part and the rotator were connected with the stator by a bearing, and the distance between them was adjusted to make the FEP film contact the copper foil on the surface of the stator.

Electrical Output Measurements. For the purpose of performance evaluation, the open-circuit voltage and short-circuit current of the TENG device were measured by a Keithley 6514 system electrometer. For the multichannel measurement and demonstration, the voltage outputs were measured by an ADC (NI 9220, 16-channel voltage measurement module, ±10 V, National Instrument).

Signal Processing and System Implementation. The signal acquisition, timing synchronization, and the graphical user interface were implemented using NI DAQ and LabVIEW 2016. Refer to Supplementary Figure 5 for details on the proposed algorithm for wind direction and speed detection.

ASSOCIATED CONTENT

Supporting Information

The Supporting Information is available free of charge on the ACS Publications website at DOI: 10.1021/acsnano.8b01532.

Figures S1−S4 (PDF)

Movie S1: Demonstration of v-TENG for reflecting the moving trail of the rotator (AVI)

Movie S2: Demonstration of wind sensor system for detecting real-time wind speed under a complete process in which the wind speed increases gradually and then gradually decreases, and a demonstration of the wind sensor system simultaneously outputting the wind speed and wind direction under a particular wind speed (AVI)

Movie S3: Demonstration of a real-time comparison between the wind sensor system and a hotwire anemometer under start-up wind speed, medium wind speed, and maximum wind speed (AVI)

AUTHOR INFORMATION

Corresponding Authors

*E-mail: rjliao@cqu.edu.cn (R.-J. Liao).

*E-mail: zhong.wang@mse.gatech.edu (Z. L. Wang).

ORCID

Lun Pan: 0000-0002-3083-4693

Zhong Lin Wang: 0000-0002-5530-0380

Author Contributions

⊥J. Wang, W. Ding, and L. Pan contributed equally to this work.

Notes

The authors declare no competing financial interest.

ACKNOWLEDGMENTS

This research was supported by the Hightower Chair Foundation, the National Key R & D Project from the Ministry of Science and Technology (2016YFA0202704, 2016YFA0202702), the National Natural Science Foundation of China (Grant Nos. 51432005, 5151101243, 51561145021), and the Chinese Scholars Council.

REFERENCES

(1) Wang, Z. On Maxwell's Displacement Current for Energy and Sensors: The Origin of Nanogenerators. *Mater. Today* **2017**, *20*, 74−82.

(2) Gubbi, J.; Buyya, R.; Marusic, S.; Palaniswami, M. Internet of Things (Iot): A Vision, Architectural Elements, and Future Directions. *Future Gener. Comp. Sy* **2013**, *29*, 1645−1660.

(3) Jiang, C.; Li, H.; Wang, C. Recent Progress in Solid-State Electrolytes for Alkali-Ion Batteries. *Chin. Sci. Bull.* **2017**, *62*, 1473−1490.

(4) Ma, F.; Li, Q.; Wang, T.; Zhang, H.; Wu, G. Energy Storage Materials Derived from Prussian Blue Analogues. *Chin. Sci. Bull.* **2017**, *62*, 358−368.

(5) Zhang, J.; Yu, A. Nanostructured Transition Metal Oxides as Advanced Anodes for Lithium-Ion Batteries. *Chin. Sci. Bull.* **2015**, *60*, 823−838.

(6) Wang, Z. Triboelectric Nanogenerators as New Energy Technology for Self-Powered Systems and as Active Mechanical and Chemical Sensors. *ACS Nano* **2013**, *7*, 9533−9557.

(7) Wang, Z.; Chen, J.; Lin, L. Progress in Triboelectric Nanogenerators as a New Energy Technology and Self-Powered Sensors. *Energy Environ. Sci.* **2015**, *8*, 2250−2282.

(8) Su, Y.; Wen, X.; Zhu, G.; Yang, J.; Chen, J.; Bai, P.; Wu, Z.; Jiang, Y.; Wang, Z. Hybrid Triboelectric Nanogenerator for Harvesting Water Wave Energy and as a Self-Powered Distress Signal Emitter. *Nano Energy* **2014**, *9*, 186−195.

(9) Niu, S.; Wang, S.; Lin, L.; Liu, Y.; Zhou, Y.; Hu, Y.; Wang, Z. Theoretical Study of Contact-Mode Triboelectric Nanogenerators as an Effective Power Source. *Energy Environ. Sci.* **2013**, *6*, 3576.

(10) Wang, S.; Lin, L.; Wang, Z. Triboelectric Nanogenerators as Self-Powered Active Sensors. *Nano Energy* **2015**, *11*, 436−462.

(11) Zhu, G.; Peng, B.; Chen, J.; Jing, Q.; Wang, Z. Triboelectric Nanogenerators as a New Energy Technology: from Fundamentals, Devices, to Applications. *Nano Energy* **2015**, *14*, 126−138.

(12) Zi, Y.; Wang, Z. Nanogenerators: An Emerging Technology towards Nanoenergy. *APL Mater.* **2017**, *5*, 074103.

(13) Wang, J.; Li, S.; Yi, F.; Zi, Y.; Lin, J.; Wang, X.; Xu, Y.; Wang, Z. Sustainably Powering Wearable Electronics Solely by Biomechanical Energy. *Nat. Commun.* **2016**, *7*, 12744.

(14) Zhong, X.; Yang, Y.; Wang, X.; Wang, Z. Rotating-Disk-Based Hybridized Electromagnetic-Triboelectric Nanogenerator for Scavenging Biomechanical Energy as a Mobile Power Source. *Nano Energy* **2015**, *13*, 771−780.

(15) Zhang, H.; Yang, Y.; Hou, T.; Su, Y.; Hu, C.; Wang, Z. Triboelectric Nanogenerator Built inside Clothes for Self-Powered Glucose Biosensors. *Nano Energy* **2013**, *2*, 1019−1024.

(16) Zhu, G.; Bai, P.; Chen, J.; Lin Wang, Z. Power-Generating Shoe Insole Based on Triboelectric Nanogenerators for Self-Powered Consumer Electronics. *Nano Energy* **2013**, *2*, 688−692.

(17) Yang, Y.; Zhu, G.; Zhang, H.; Chen, J.; Zhong, X.; Lin, Z.; Su, Y.; Bai, P.; Wen, X.; Wang, Z. Triboelectric Nanogenerator for Harvesting Wind Energy and as Self-Powered Wind Vector Sensor System. *ACS Nano* **2013**, *7*, 9461−9468.

(18) Xie, Y.; Wang, S.; Lin, L.; Jing, Q.; Lin, Z.; Niu, S.; Wu, Z.; Wang, Z. Rotary Triboelectric Nanogenerator Based on a Hybridized Mechanism for Harvesting Wind Energy. *ACS Nano* **2013**, *7*, 7119−7125.

(19) Chen, S.; Gao, C.; Tang, W.; Zhu, H.; Han, Y.; Jiang, Q.; Li, T.; Cao, X.; Wang, Z. Self-Powered Cleaning of Air Pollution by Wind Driven Triboelectric Nanogenerator. *Nano Energy* **2015**, *14*, 217−225.

(20) Wang, Z.; Jiang, T.; Xu, L. Toward the Blue Energy Dream by Triboelectric Nanogenerator Networks. *Nano Energy* **2017**, *39*, 9−23.

(21) Wang, Z. Catch Wave Power in Floating Nets. *Nature* **2017**, *542*, 159−160.

DOI: 10.1021/acsnano.8b01532
ACS Nano XXXX, XXX, XXX−XXX

(22) Chen, J.; Yang, J.; Li, Z.; Fan, X.; Zi, Y.; Jing, Q.; Guo, H.; Wen, Z.; Pradel, K.; Niu, S.; Wang, Z. Networks of Triboelectric Nanogenerators for Harvesting Water Wave Energy: A Potential Approach Toward Blue Energy. *ACS Nano* **2015**, *9*, 3324−3331.
(23) Zhang, L.; Han, C.; Jiang, T.; Zhou, T.; Li, X.; Zhang, C.; Wang, Z. Multilayer Wavy-Structured Robust Triboelectric Nanogenerator for Harvesting Water Wave Energy. *Nano Energy* **2016**, *22*, 87−94.
(24) Pan, L.; Wang, J.; Wang, P.; Gao, R.; Wang, Y.; Zhang, X.; Zou, J.; Wang, Z. Liquid-FEP-Based U-Tube Triboelectric Nanogenerator for Harvesting Water-Wave Energy. *Nano Res.* **2018**, 10.1007/s12274-018-1989-9.
(25) Wang, X.; Niu, S.; Yin, Y.; Yi, F.; You, Z.; Wang, Z. Triboelectric Nanogenerator Based on Fully Enclosed Rolling Spherical Structure for Harvesting Low-Frequency Water Wave Energy. *Adv. Energy Mater.* **2015**, *5*, 1501467.
(26) Zi, Y.; Guo, H.; Wen, Z.; Yeh, M.; Hu, C.; Wang, Z. Harvesting Low-Frequency (<5 Hz) Irregular Mechanical Energy: A Possible Killer Application of Triboelectric Nanogenerator. *ACS Nano* **2016**, *10*, 4797−4805.
(27) Wu, C.; Liu, R.; Wang, J.; Zi, Y.; Lin, L.; Wang, Z. A Spring-Based Resonance Coupling for Hugely Enhancing the Performance of Triboelectric Nanogenerators for Harvesting Low-Frequency Vibration Energy. *Nano Energy* **2017**, *32*, 287−293.
(28) Zheng, Q.; Jin, Y.; Liu, Z.; Ouyang, H.; Li, H.; Shi, B.; Jiang, W.; Zhang, H.; Li, Z.; Wang, Z. Robust Multilayered Encapsulation for High-Performance Triboelectric Nanogenerator in Harsh Environment. *ACS Appl. Mater. Interfaces* **2016**, *8*, 26697−26703.
(29) Zhong, J.; Zhong, Q.; Chen, G.; Hu, B.; Zhao, S.; Li, X.; Wu, N.; Li, W.; Yu, H.; Zhou, J. Surface Charge Self-Recovering Electret Film for Wearable Energy Conversion in a Harsh Environment. *Energy Environ. Sci.* **2016**, *9*, 3085−3091.
(30) Xi, Y.; Guo, H.; Zi, Y.; Li, X.; Wang, J.; Deng, J.; Li, S.; Hu, C.; Cao, X.; Wang, Z. Multifunctional TENG for Blue Energy Scavenging and Self-Powered Wind-Speed Sensor. *Adv. Energy Mater.* **2017**, *7*, 1602397.
(31) Xie, Y.; Wang, S.; Niu, S.; Lin, L.; Jing, Q.; Su, Y.; Wu, Z.; Wang, Z. Multi-Layered Disk Triboelectric Nanogenerator for Harvesting Hydropower. *Nano Energy* **2014**, *6*, 129−136.
(32) Zhang, X.; Han, M.; Meng, B.; Zhang, H. High Performance Triboelectric Nanogenerators Based on Large-Scale Mass-Fabrication Technologies. *Nano Energy* **2015**, *11*, 304−322.
(33) Wang, X.; Wang, Z.; Yang, Y. Hybridized Nanogenerator for Simultaneously Scavenging Mechanical and Thermal Energies by Electromagnetic-Triboelectric-Thermoelectric Effects. *Nano Energy* **2016**, *26*, 164−171.
(34) Li, S.; Wang, S.; Zi, Y.; Wen, Z.; Lin, L.; Zhang, G.; Wang, Z. Largely Improving the Robustness and Lifetime of Triboelectric Nanogenerators through Automatic Transition between Contact and Noncontact Working States. *ACS Nano* **2015**, *9*, 7479−7487.
(35) Moon, H.; Chung, J.; Kim, B.; Yong, H.; Kim, T.; Lee, S.; Lee, S. Stack/Flutter-Driven Self-Retracting Triboelectric Nanogenerator for Portable Electronics. *Nano Energy* **2017**, *31*, 525−532.
(36) Seol, M.; Woo, J.; Jeon, S.; Kim, D.; Park, S.; Hur, J.; Choi, Y. Vertically Stacked Thin Triboelectric Nanogenerator for Wind Energy Harvesting. *Nano Energy* **2015**, *14*, 201−208.
(37) Bae, J.; Lee, J.; Kim, S.; Ha, J.; Lee, B.; Park, Y.; Choong, C.; Kim, J.; Wang, Z.; Kim, H.; Park, J.; Chung, U. Flutter-Driven Triboelectrification for Harvesting Wind Energy. *Nat. Commun.* **2014**, *5*, 4929.
(38) Zhao, Z.; Pu, X.; Du, C.; Li, L.; Jiang, C.; Hu, W.; Wang, Z. Freestanding Flag-Type Triboelectric Nanogenerator for Harvesting High-Altitude Wind Energy from Arbitrary Directions. *ACS Nano* **2016**, *10*, 1780−1787.
(39) Jiang, T.; Chen, X.; Han, C.; Tang, W.; Wang, Z. Theoretical Study of Rotary Freestanding Triboelectric Nanogenerators. *Adv. Funct. Mater.* **2015**, *25*, 2928−2938.
(40) Wang, S.; Xie, Y.; Niu, S.; Lin, L.; Wang, Z. Freestanding Triboelectric-Layer-Based Nanogenerators for Harvesting Energy from a Moving Object or Human Motion in Contact and Non-Contact Modes. *Adv. Mater.* **2014**, *26*, 2818−2824.
(41) Mao, Y.; Geng, D.; Liang, E.; Wang, X. Single-Electrode Triboelectric Nanogenerator for Scavenging Friction Energy from Rolling Tires. *Nano Energy* **2015**, *15*, 227−234.
(42) Yang, Y.; Zhang, H.; Chen, J.; Jing, Q.; Zhou, Y.; Wen, X.; Wang, Z. Single-Electrode-Based Sliding Triboelectric Nanogenerator for Self-Powered Displacement Vector Sensor System. *ACS Nano* **2013**, *7*, 7342−7351.
(43) Zhu, G.; Chen, J.; Zhang, T.; Jing, Q.; Wang, Z. Radial-Arrayed Rotary Electrification for High Performance Triboelectric Generator. *Nat. Commun.* **2014**, *5*, 5.
(44) Wang, S.; Xie, Y.; Niu, S.; Lin, L.; Liu, C.; Zhou, Y.; Wang, Z. Maximum Surface Charge Density for Triboelectric Nanogenerators Achieved by Ionized-Air Injection: Methodology and Theoretical Understanding. *Adv. Mater.* **2014**, *26*, 6720−6728.

DOI: 10.1021/acsnano.8b01532
ACS Nano XXXX, XXX, XXX−XXX